PHYSICAL REVIEW A **95**, 062103 (2017)

Suppression of the cross-talk effect in a dual-axis K-Rb-^{21}Ne comagnetometer

Liwei Jiang,[*] Wei Quan,[†] Rujie Li, Lihong Duan, Wenfeng Fan, Zhuo Wang, Feng Liu, Li Xing, and Jiancheng Fang
School of Instrument Science and Opto-Electronics Engineering, Beihang University, Beijing 100191, People's Republic of China

(Received 31 December 2016; published 2 June 2017)

A compact dual-axis K-Rb-^{21}Ne comagnetometer with one circularly polarized pump beam and two orthogonal linearly polarized probe beams is presented. It can be exploited for rotation sensing by operating in the spin-exchange relaxation-free regime. Due to the light shift arising from the pump laser, there is a cross-talk effect between the two sensitive axes, which limits the comagnetometer applications. To eliminate this effect, an external field parallel to the direction of the pump beam is used to compensate the light-shift field. It is validated theoretically and experimentally in the dual-axis K-Rb-^{21}Ne comagnetometer. With the cross-talk effect suppressed, the comagnetometer can carry out high-precision rotation sensing along two sensitive axes simultaneously and independently.

DOI: 10.1103/PhysRevA.95.062103

I. INTRODUCTION

An alkali metal–noble gas comagnetometer operating in the spin-exchange relaxation-free (SERF) regime has been investigated quite intensively [1,2] and found a wide range of applications, from tests of Lorentz and CPT violation [3,4] to searches for anomalous spin forces [5,6]. Furthermore, it can be exploited for rotation sensing as gyroscope [7,8]. In the SERF atomic spin comagnetometer, the sensitivity of the magnetic field is highly suppressed by interactions between alkali metal and noble gas, leaving only a signal proportional to rotations and other anomalous fields [9]. This comagnetometer is promising as a compact, low-cost, and high-precision inertial sensor for future navigation applications [10].

A SERF atomic spin comagnetometer sensing rotations based on K-^{3}He was first demonstrated in 2005, achieving a rotation sensitivity of 5.0×10^{-7} rad s^{-1} Hz$^{-1/2}$ [8]. Since then, a sensitivity of 1.2×10^{-6} rad s^{-1} Hz$^{-1/2}$ was achieved by a Cs-^{129}Xe comagnetometer [11,12] and a Rb-^{129}Xe pair was also utilized in a comagnetometer arrangement for rotation sensing [13]. Because the gyromagnetic ratio of ^{21}Ne is about 10 times lower than that of ^{3}He and about 3 times lower than that of ^{129}Xe, the predicted rotation sensitivity of the ^{21}Ne comagnetometer is about 10 times higher than that of the ^{3}He comagnetometer and 3 times higher than that of the ^{129}Xe comagnetometer [8,14]. But the electric quadrupole interactions of ^{21}Ne cause a faster nuclear spin relaxation. Rb atoms have advantages over other alkali metals, mainly owing to having a larger spin-exchange cross section with ^{21}Ne [15]. The K-Rb hybrid pumping technique is utilized to overcome strong absorption of the pump laser by the optically dense Rb vapor [16,17] and then to achieve more homogeneous polarization. By optimizing the laser power and cell temperature, a rotation sensitivity of 2.1 $\times 10^{-8}$ rad s^{-1} Hz$^{-1/2}$ was achieved by the K-Rb-^{21}Ne comagnetometer [18].

The SERF atomic spin comagnetometer utilizes alkali metal and noble gas overlapping spin ensembles to sense rotations, which is much more similar to a traditional mechanical gyroscope. The traditional mechanical gyroscope can work as a dual-axis gyroscope to sense rotations orthogonal to the spin mass direction [19]. Similarly, the SERF atomic spin comagnetometer can sense the rotations in two axes orthogonal to the polarization of spin ensembles [20]. We report on a compact dual-axis K-Rb-^{21}Ne comagnetometer which is different from the apparatuses mentioned above with a large volume and single sensitive axis. However, the light shift arising from the circularly polarized pump laser in the K-Rb-^{21}Ne comagnetometer causes a severe cross-talk effect between the two sensitive axes [10]. Here, a method using an external field to compensate the light-shift field is proposed to reduce the cross-talk effect. We investigate the steady-state response of the electron and nuclear spin polarizations and give an intuitive model to explain the cross-talk effect and its suppression. The feasibility is emphasized and verified by experiments. With the cross-talk effect eliminated, the dual-axis K-Rb-^{21}Ne comagnetometer can carry out high-precision rotation sensing along two sensitive axes simultaneously and independently.

II. THEORY OF THE CROSS-TALK EFFECT AND ITS SUPPRESSION

The coupled dynamics of the comagnetometer can be approximated by a set of Bloch equations [8]. In the K-Rb-^{21}Ne comagnetometer, as the Rb atom number density is much higher than the K atom number density, it is a proper approximation to consider only the electron polarization of the Rb atom [7]. The evolutions of the electron spin polarization $\mathbf{P^e}$ and nuclear spin polarization $\mathbf{P^n}$ are as follows:

$$\begin{aligned}\frac{\partial \mathbf{P^e}}{\partial t} &= \Omega \times \mathbf{P^e} + \frac{\gamma_e}{Q}(\mathbf{B} + \lambda M_n \mathbf{P^n} + \mathbf{L}) \times \mathbf{P^e} \\ &\quad + \frac{1}{Q}\left(R_{\rm pu}\mathbf{s_{pu}} + R_m \mathbf{s_{pr}} + R_{se}^{en}\mathbf{P^n} - R_{\rm tot}^{e}\mathbf{P^e}\right), \\ \frac{\partial \mathbf{P^n}}{\partial t} &= \Omega \times \mathbf{P^n} + \gamma_n(\mathbf{B} + \lambda M_e \mathbf{P^e}) \times \mathbf{P^n} \\ &\quad + R_{se}^{ne}(\mathbf{P^e} - \mathbf{P^n}) - R_{sd}^{n}\mathbf{P^n}. \end{aligned} \qquad (1)$$

The above Bloch equations are written in the rotating frame. Where Ω is the inertial rotation rate vector. γ_e and γ_n are the gyromagnetic ratios of the electron and nuclear

---

[*] Jiangliwei@buaa.edu.cn

[†] quanwei@buaa.edu.cn

spins, respectively. Q is the electron slowing-down factor due to hopping between hyperfine levels. $\lambda = 8\pi\kappa_0/3$ is the geometrical factor containing the enhancement factor [21], while M_e and M_n are the magnetizations of electron and nuclear spins corresponding to full spin polarization. The electron spins precess in the ambient magnetic field $\mathbf{B}$, the magnetization of the nuclear spins $\lambda M_n \mathbf{P^n}$, and the light shift $\mathbf{L}$. Similarly, the nuclear spins precess in the ambient magnetic field $\mathbf{B}$ and the magnetization of the electron spins $\lambda M_e \mathbf{P^e}$. Note that $\mathbf{L}$ is the light shift (ac-Stark shift) field arising from the pump and probe lasers [22,23], which presents itself as a fictitious magnetic field coupling only to electrons. The second line of each equation contains the various pumping and relaxation rates. R_{pu} and R_m are the pumping rates of the pump and probe laser beams. $\mathbf{s_{pu}}$ and $\mathbf{s_{pr}}$ are the optical pumping vectors, which give the directions and magnitudes of the photon spin polarizations. R_{se}^{en} and R_{se}^{ne} are the spin-exchange rates of the electron and the nucleus with each other. R_{tot}^{e} is the total spin-relaxation rate for electron, defined as $R_{\mathrm{tot}}^{e} = R_{\mathrm{pu}} + R_m + R_{\mathrm{se}}^{en} + R_{\mathrm{sd}}^{e}$, where R_{sd}^{e} is the electron spin-destruction rate. R_{sd}^{n} is the nuclear spin-destruction rate.

As the equilibrium polarization vectors of electron and nuclear spins are oriented along the z axis, the same direction as the pump beam under a nominal comagnetometer configuration, we approximately assume the longitudinal polarization components P_z^e and P_z^n to be constants, which are not affected by the presence of transverse components. The steady-state solution of the Bloch equations can be derived by setting the left-hand side of Eq. (1) to 0. The leading terms of transverse electron spin polarization P_x^e and P_y^e with exquisite refinement are expressed by Eqs. (2) and (3), while P_x^n and P_y^n are expressed by Eqs. (4) and (5):

$$
\begin{aligned}
P_x^e = {} & \frac{\gamma_e P_z^e}{{R_{\mathrm{tot}}^{e}}^2 + {\gamma_e}^2\big[\delta B_z + L_z - \frac{\Omega_z}{\gamma} - \frac{\delta B_z B_e}{\delta B_z - B_n}\big]^2} \Bigg\{ \Bigg[\frac{(\delta B_z + L_z - \Omega_z/\gamma)(B_n\gamma_e - B_n Q\gamma_n + Q\gamma_n\delta B_z)}{\gamma_n(\delta B_z - B_n)} - \frac{Q\delta B_z B_e}{\delta B_z - B_n} \\
& - \frac{\gamma_e \delta B_z B_e B_n}{\gamma_n(\delta B_z - B_n)^2} \Bigg] \Omega_x + \frac{(B_n\gamma_e - B_n Q\gamma_n + Q\gamma_n\delta B_z)R_{\mathrm{tot}}^{e}}{\gamma_e\gamma_n(\delta B_z - B_n)} \Omega_y + \left[\frac{\delta B_z + L_z - \Omega_z/\gamma}{\delta B_z - B_n} - \frac{\delta B_z B_e}{(\delta B_z - B_n)^2} \right] \gamma_e \delta B_z B_x \\
& + \frac{R_{\mathrm{tot}}^{e}\delta B_z}{\delta B_z - B_n} B_y + \left[\delta B_z + L_z - \frac{\Omega_z}{\gamma} - \frac{\delta B_z B_e}{\delta B_z - B_n} \right] \gamma_e L_x + R_{\mathrm{tot}}^{e} L_y \Bigg\},
\end{aligned} \tag{2}
$$

$$
\begin{aligned}
P_y^e = {} & \frac{\gamma_e P_z^e}{{R_{\mathrm{tot}}^{e}}^2 + {\gamma_e}^2\big[\delta B_z + L_z - \frac{\Omega_z}{\gamma} - \frac{\delta B_z B_e}{\delta B_z - B_n}\big]^2} \Bigg\{ - \frac{(B_n\gamma_e - B_n Q\gamma_n + Q\gamma_n\delta B_z)R_{\mathrm{tot}}^{e}}{\gamma_e\gamma_n(\delta B_z - B_n)} \Omega_x \\
& + \left[\frac{(\delta B_z + L_z - \Omega_z/\gamma)(B_n\gamma_e - B_n Q\gamma_n + Q\gamma_n\delta B_z)}{\gamma_n(\delta B_z - B_n)} - \frac{Q\delta B_z B_e}{\delta B_z - B_n} - \frac{\gamma_e \delta B_z B_e B_n}{\gamma_n(\delta B_z - B_n)^2} \right] \Omega_y - \frac{R_{\mathrm{tot}}^{e}\delta B_z}{\delta B_z - B_n} B_x \\
& + \left[\frac{\delta B_z + L_z - \Omega_z/\gamma}{\delta B_z - B_n} - \frac{\delta B_z B_e}{(\delta B_z - B_n)^2} \right] \gamma_e \delta B_z B_y - R_{\mathrm{tot}}^{e} L_x + \left[\delta B_z + L_z - \frac{\Omega_z}{\gamma} - \frac{\delta B_z B_e}{\delta B_z - B_n} \right] \gamma_e L_y \Bigg\},
\end{aligned} \tag{3}
$$

$$
\begin{aligned}
P_x^n = {} & \frac{P_z^n}{\gamma_n(\delta B_z - B_n)\big[{R_{\mathrm{tot}}^{e}}^2 + {\gamma_e}^2\big(\delta B_z + L_z - \frac{\Omega_z}{\gamma} - \frac{\delta B_z B_e}{\delta B_z - B_n}\big)^2\big]} \\
& \times \Bigg\{ \Bigg[{R_{\mathrm{tot}}^{e}}^2 + {\gamma_e}^2 \left(\delta B_z + L_z - \frac{\Omega_z}{\gamma} - B_e \right) \left(\delta B_z + L_z - \frac{\Omega_z}{\gamma} - \frac{\delta B_z B_e}{\delta B_z - B_n} \right) \\
& + \gamma_e\gamma_n Q B_e \left(\delta B_z + L_z - \frac{\Omega_z}{\gamma} \right) - \frac{\gamma_e\gamma_n Q \delta B_z B_e^2}{\delta B_z - B_n} \Bigg] \Omega_x + \frac{(\gamma_e B_n + Q\gamma_n\delta B_z - Q\gamma_n B_n)R_{\mathrm{tot}}^{e} B_e}{\delta B_z - B_n} \Omega_y \\
& + \left[{R_{\mathrm{tot}}^{e}}^2 + {\gamma_e}^2 \left(\delta B_z + L_z - \frac{\Omega_z}{\gamma} \right) \left(\delta B_z + L_z - \frac{\Omega_z}{\gamma} - \frac{\delta B_z B_e}{\delta B_z - B_n} \right) \right] \gamma_n B_x + \frac{\gamma_e\gamma_n R_{\mathrm{tot}}^{e} \delta B_z B_e}{\delta B_z - B_n} B_y \\
& + \left[\delta B_z + L_z - \frac{\Omega_z}{\gamma} - \frac{\delta B_z B_e}{\delta B_z - B_n} \right] \gamma_e^2 \gamma_n B_e L_x + \gamma_e\gamma_n R_{\mathrm{tot}}^{e} B_e L_y \Bigg\},
\end{aligned} \tag{4}
$$

$$
\begin{aligned}
P_y^n = {} & \frac{P_z^n}{\gamma_n(\delta B_z - B_n)\big[{R_{\mathrm{tot}}^{e}}^2 + {\gamma_e}^2\big(\delta B_z + L_z - \frac{\Omega_z}{\gamma} - \frac{\delta B_z B_e}{\delta B_z - B_n}\big)^2\big]} \\
& \times \Bigg\{ - \frac{(\gamma_e B_n + Q\gamma_n\delta B_z - Q\gamma_n B_n)R_{\mathrm{tot}}^{e} B_e}{\delta B_z - B_n} \Omega_x + \Bigg[{R_{\mathrm{tot}}^{e}}^2 + \gamma_e\gamma_n Q B_e \left(\delta B_z + L_z - \frac{\Omega_z}{\gamma} \right) \\
& - \frac{\gamma_e\gamma_n Q \delta B_z B_e^2}{\delta B_z - B_n} + {\gamma_e}^2 \left(\delta B_z + L_z - \frac{\Omega_z}{\gamma} - B_e \right) \left(\delta B_z + L_z - \frac{\Omega_z}{\gamma} - \frac{\delta B_z B_e}{\delta B_z - B_n} \right) \Bigg] \Omega_y
\end{aligned}
$$

$$-\frac{\gamma_e\gamma_n R_{\rm tot}^e\delta B_z B_e}{\delta B_z - B_n}B_x + \left[{R_{\rm tot}^e}^2 + {\gamma_e}^2\left(\delta B_z + L_z - \frac{\Omega_z}{\gamma}\right)\left(\delta B_z + L_z - \frac{\Omega_z}{\gamma} - \frac{\delta B_z B_e}{\delta B_z - B_n}\right)\right]\gamma_n B_y$$
$$-\gamma_e\gamma_n R_{\rm tot}^e B_e L_x + \left[\delta B_z + L_z - \frac{\Omega_z}{\gamma} - \frac{\delta B_z B_e}{\delta B_z - B_n}\right]\gamma_e^2\gamma_n B_e L_y\Bigg\}, \tag{5}$$

where $\gamma = \gamma_e\gamma_n/(\gamma_e - Q\gamma_n)$. Under normal comagnetometer operation, a bias field $B_c = -B_n - B_e$ called the compensation point is applied to the z axis to cancel the field from nuclear magnetization $B_n = \lambda M_n P_z^n$ and the field from electron magnetization $B_e = \lambda M_e P_z^e$. δB_z is the magnetic field with respect to the compensation point. With the residual magnetic field of the magnetic shields compensated by coils, δB_z approaches 0 at the compensation point.

In the K-Rb-^{21}Ne comagnetometer, the magnetic field B_n produced by nuclear magnetization is typically on the order of several hundred nT, and the magnetic field B_e produced by electron magnetization is about dozens of nT, which is much larger than that with the K-^{3}He comagnetometer. The field from electron magnetization in the compensation field cannot be neglected [7,14]. Here the steady-state response considering the field from electron magnetization is presented, which is different from previous studies [8,10]. The large field from electron magnetization B_e changes the dynamics of the electron and nuclear spin ensembles. From Eqs. (2)–(5), we can see that electron magnetization causes high-order imperfections in the response of electron spin polarization, which will become an error source when distributing the comagnetometer error in detail. Moreover, electron magnetization has a significant influence on the response of nuclear spin polarization. L_x and L_y can be set to 0, because the light shift is proportional to the circular polarization degree of the laser and the probe laser beam is linearly polarized. Since $\delta B_z \ll B_n$ and $\Omega_z/\gamma \approx 0$, Eqs. (4) and (5) can be simplified to

$$P_x^n = \frac{-P_z^n}{B_n}\left\{\left[\frac{1}{\gamma_n} - \frac{{\gamma_e}^2 B_e(\delta B_z + L_z)}{\gamma D_s}\right]\Omega_x - \frac{\gamma_e R_{\rm tot}^e B_e}{\gamma D_s}\Omega_y + B_x\right\}, \tag{6}$$

$$P_y^n = \frac{-P_z^n}{B_n}\left\{\frac{\gamma_e R_{\rm tot}^e B_e}{\gamma D_s}\Omega_x + \left[\frac{1}{\gamma_n} - \frac{{\gamma_e}^2 B_e(\delta B_z + L_z)}{\gamma D_s}\right]\Omega_y + B_y\right\}, \tag{7}$$

where $D_s = {R_{\rm tot}^e}^2 + {\gamma_e}^2(\delta B_z + L_z)^2$. In Eq. (6), with a typical experimental value of each parameter assigned in the K-Rb-^{21}Ne comagnetometer, the magnitude of the Ω_y term is comparable to that of the Ω_x term due to the large magnetization of electron B_e. When inputting a rotation along the y axis, P_x^n cannot remain stationary and both P_x^n and P_y^n will react to the rotation. The same result holds when inputting a rotation along the x axis.

The SERF atomic spin comagnetometer is usually configured with a circularly polarized pump laser beam along the z axis and a linearly polarized probe laser beam along the x axis, then the signal proportional to P_x^e is measured. In this paper, we introduce a second probe laser beam along the y axis, and the signal proportional to P_y^e is measured simultaneously. The residual magnetic fields in the x and y directions are overwhelmingly shielded and compensated. Furthermore, from Eqs. (2) and (3) it can be seen that the sensitivity of the comagnetometer signal to magnetic fields is suppressed compared to the rotations. Therefore the sensitivity to magnetic fields can be neglected in gyroscope applications. Using the same assumption as simplification of the steady-state nuclear spin polarization, Eqs. (2) and (3) can be simplified to the following illuminating form:

$$P_x^e = \frac{-\gamma_e P_z^e R_{\rm tot}^e}{D_s} \times \left[\frac{\Omega_y}{\gamma} + \frac{\gamma_e\Omega_x}{\gamma R_{\rm tot}^e}(\delta B_z + L_z)\right], \tag{8}$$

$$P_y^e = \frac{\gamma_e P_z^e R_{\rm tot}^e}{D_s} \times \left[\frac{\Omega_x}{\gamma} - \frac{\gamma_e\Omega_y}{\gamma R_{\rm tot}^e}(\delta B_z + L_z)\right]. \tag{9}$$

In the K-Rb-^{21}Ne comagnetometer, the light shift arising from the circularly polarized pump beam is on the order of a few nT, which cannot be ignored. From Eqs. (8) and (9), it is easy to see that the nonzero light shift L_z introduces a cross-talk effect on the rotation sensing, where the output signals of both sensitive axes cannot distinguish the rotations of Ω_x and Ω_y, which limits the application of the comagnetometer and serves as a source of error.

For illustrative purposes, the electron and nuclear polarizations in the K-Rb-^{21}Ne comagnetometer are estimated from Eqs. (2)–(5) by assigning an empirical value to each parameter and an intuitive model is presented in Fig. 1. When there is no rotation or other anomalous fields being input, the equilibrium polarizations for $\mathbf{P^e}$ and $\mathbf{P^n}$ are just oriented along the z axis. When a rotation is input along the y axis, $\mathbf{P^n}$ will follow the net projection of both the rotation and the magnetic fields, then slightly precess away from the z axis and induce a reaction of nuclear spin polarization along the y axis P_y^n. Meanwhile, the large electron magnetization in the K-Rb-^{21}Ne comagnetometer will induce a reaction of nuclear

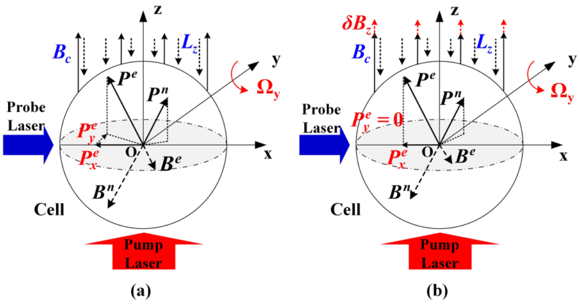

FIG. 1. Basic operation of K-Rb-^{21}Ne comagnetometer sensing Ω_y. (a) At the compensation point, the projection of $\mathbf{P^e}$ in the $x - y$ plane stabilizes at an angle to the x axis, causing a cross-talk effect in the y-axis response. (b) At the working point, with L_z compensated, the projection of $\mathbf{P^e}$ in the $x - y$ plane just aligns with the x axis, and the cross-talk effect is eliminated. The same model holds for Ω_x inputting.

spin polarization along the x axis P_x^n and pull $\mathbf{P^n}$ away from the $y-z$ plane. From the point of view of electron spins, the magnetization of nuclear spins is uncompensated and provides a real magnetic field for electrons to precess under. Here we assume that the sign of the light-shift field is negative. At the compensation point, $\mathbf{P^e}$ will follow the net projection of rotation, magnetic fields, and light-shift field, then produce a projection onto the $x-y$ plane, which is shown in Fig. 1(a). Note that due to the nonnegligible light shift L_z, the projection of $\mathbf{P^e}$ in the $x-y$ plane will stabilize at an angle to the x axis, causing a cross-talk effect of Ω_y sensing in the y-axis response.

The cross-talk effect limits inertial rotation sensing and fundamental physics applications of the comagnetometer. Hence, in this paper, we apply an opposite real magnetic field on the z axis to compensate the fictitious magnetic field of the light shift. From Eqs. (8) and (9), we can easily see that by setting $\delta B_z = -L_z$, the cross-talk effect is totally eliminated. Since $\delta B_z = 0$ is referred to as the compensation point in Ref. [9], we refer to $\delta B_z = -L_z$ as the working point of the K-Rb-^{21}Ne comagnetometer. An illustrative model is shown in Fig. 1(b). As L_z is compensated by δB_z, the projection of $\mathbf{P^e}$ in the $x-y$ plane just aligns with the x axis, only inducing response on the x axis. P_y^e is equal to 0 and there is no response on the y axis when sensing Ω_y. The same model holds for inputting Ω_x.

III. EXPERIMENTAL SETUP AND RESULTS

A schematic of the compact dual-axis K-Rb-^{21}Ne comagnetometer is shown in Fig. 2. A 10-mm-diameter spherical cell made from GE180 aluminosilicate glass, containing a mixture of K and Rb (72.2% ^{85}Rb and 27.8% ^{87}Rb) alkali metals, 2.7 atm of ^{21}Ne (70% isotope enriched), and 61 Torr of N_2 for quenching, is used. The glass cell is placed in a boron nitride ceramic oven, which is heated with a homemade 100-kHz ac electrical heater. The operating temperature of the cell is 200°C, at which the density ratio of K to Rb is approximately 1:130. Four layers of high μ-mental cylindrical magnetic shields surround the assembly, providing a shielding factor of about 10^6 to the quasistatic magnetic fields. A set of three-axis Helmholtz coils is used to compensate and control the magnetic fields inside the shields [24].

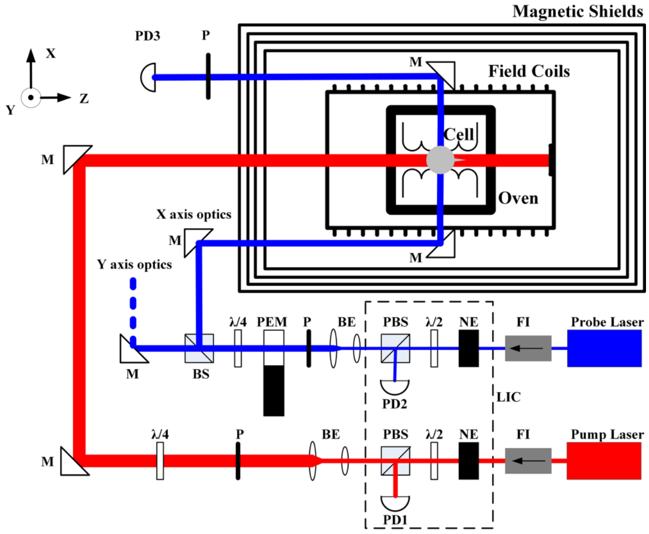

FIG. 2. Schematic of our compact dual-axis comagnetometer without the signal processing and controlling system (not shown). The external dimension of the comagnetometer is $360 \times 340 \times 260$ mm^3. FI, Faraday isolator; NE, noise eater; PBS, polarization beam splitter; BE, beam expander; P, linear polarizer; PEM, photoelastic modulator; BS, beam splitter; PD, photodiode; M, reflection mirror; LIC, laser intensity controller. The Y-axis optics are similar to the X-axis optics and the parts into the page are not shown completely.

K atoms are optically pumped along the z axis by a circularly polarized laser using about 70 mW emitted from an external cavity diode laser tuned to the K D1 resonance line at 770.1 nm. The Gaussian beam is expanded by a set of beam expanders and the relatively uniform light intensity area is selected to cover the whole cell, which reduces the inhomogeneity of light shift. Rb atoms are polarized by the K atoms through spin exchange interaction, then they hyperpolarize the ^{21}Ne atoms.

When sensing rotations, the polarizations of electron and nuclear spin will precess slightly away from the z axis and produce a projection in the transverse direction. The transverse polarization of Rb vapor is measured by the optical rotation of a linearly polarized probe beam using about 1 mW, which is emitted from a distributed feedback laser tuned by about 0.3 nm to the blue of the D1 resonance line. The Gaussian beam is expanded by a set of beam expanders to 3-mm diameter and split by a beam splitter to measure the transverse polarization in the x direction and y direction, respectively. The measurement sensitivity is enhanced by adopting a photoelastic modulation technique [25,26]. The first linear polarizer determines the initial polarization axis at 0°. The quarter-wave plate and the photoelastic modulator are oriented at 0° and 45°, respectively and the final linear polarizer acts as an analyzer at 90°. The phase retardation of the photoelastic modulator is modulated at $f = 84$ kHz, determined by the property of itself, with a modulation amplitude of $\alpha = 0.1$ rad. A homemade laser intensity controller sampling the signal of photodiodes (PD1 and PD2) stabilizes the power of the pump laser and probe laser using the noise eater as an actuator, which guarantees long-term stability.

The comagnetometer is placed on a rotating platform which can provide stable rotation input with an accuracy of 0.001 deg/s. The y axis of the comagnetometer is mounted vertically and aligned with the rotating axis of the platform. This features the calibration of the comagnetometer we built.

As shown in Fig. 1, when the dual-axis comagnetometer is operating at the working point, the cross-talk effect arising from the light shift will be suppressed. According to Eq. (9), the signal in the y-axis optics response to Ω_y modulation as a function of δB_z has a standard dispersion shape. When $\partial P_y^e/\partial\Omega_y$ equals 0, δB_z equals $-L_z$, which is the working point. Here we define that when inputting the rotation rate along the y axis, the signal measured in the y-axis optics is the coupling response, and the signal measured in the x-axis optics is the sensitive response. A step rotation $\Delta\Omega_y = 0.1$ deg/s is applied by the rotating platform. Then the coupling response in the y-axis probe optics is measured and fitted by Eq. (9), which is shown in Fig. 3, where A is the compensation

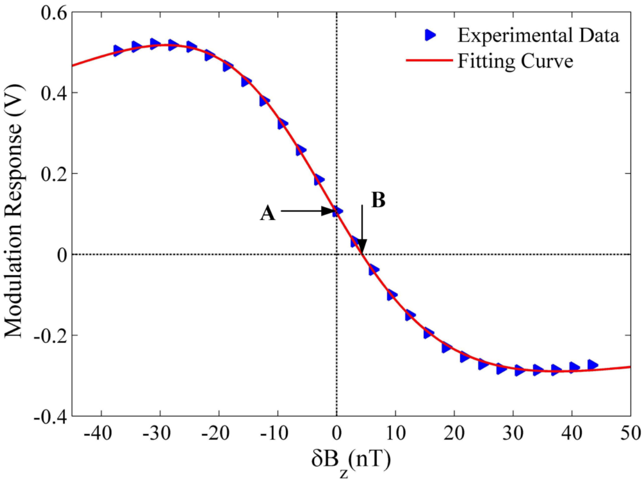

FIG. 3. The comagnetometer response measured in y-axis optics (coupling response) to Ω_y modulation as a function of δB_z. A is the compensation point, while B is the working point.

point and B is the working point, with $\delta B_z = -L_z = 4.294$ nT. The measured light shift is very consistent with the result of the B_y modulation method in Ref. [7], within the error due to the minor terms discarded in Eq. (3).

The performance of the cross-talk effect suppression at the working point is validated in Fig. 4. Rotation rates varying from -1 to 1 deg/s are input along the y axis, and the coupling response of the dual-axis comagnetometer is measured. The linear range of the comagnetometer response is about -0.6 to 0.6 deg/s. This is because when the inputting rotation rate is increasing, the assumption in Sec. II that the longitudinal components P_z^e and P_z^n are not affected by the transverse components is not positive. When the comagnetometer is operating at the compensation point, the cross-talk effect is severe. The scale factor of the coupling response in the linear range is $-0.929\ \mathrm{V/(deg\,s^{-1})}$, while the scale factor of the sensitive response is now $4.430\ \mathrm{V/(deg\,s^{-1})}$. The coupling coefficient is up to 21%, which is often an undesirable feature of the comagnetometer and limits its practical applications. When the comagnetometer is operating at the working point where δB_z is set to 4.294 nT, the coupling response is completely eliminated in the linear range, but the sensitive response is retained. When the light-shift field is overcompensated, the coupling response is reversed, which agrees well with the theory.

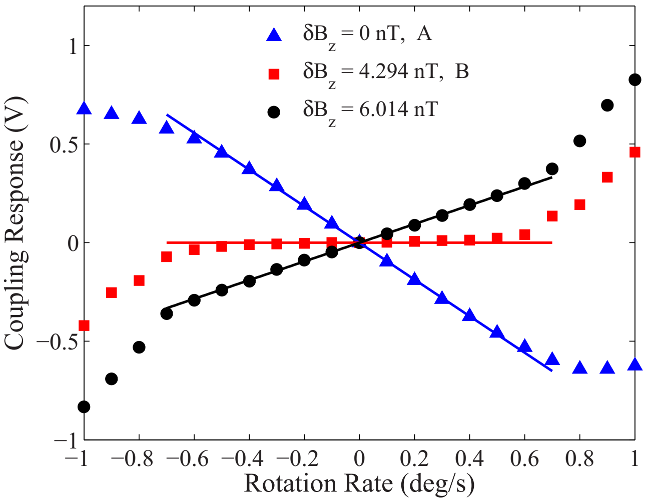

FIG. 4. Coupling response measured in the y-axis optics when inputting different Ω_y's. At the compensation point (triangles), the cross-talk effect is severe. At the working point (squares), the cross-talk effect is completely suppressed in the linear range. When the light-shift field is overcompensated (circles), the coupling response is reversed.

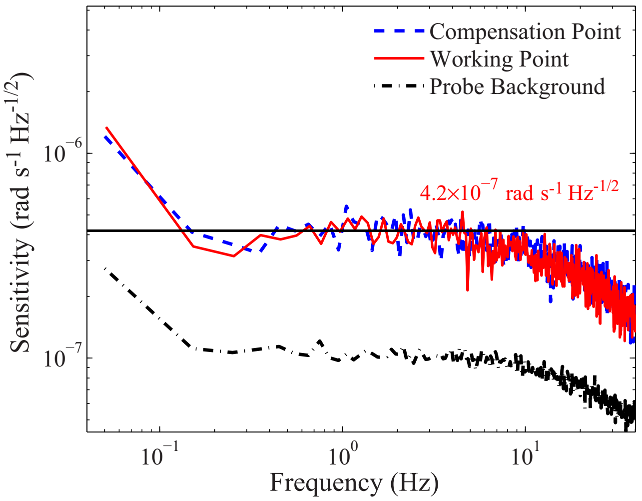

FIG. 5. Rotation sensitivity of the comagnetometer operating at the compensation point and the working point. The probe background noise obtained in the absence of a pump laser is also shown. The sensitivity of the two sensitive axes is the same.

In Fig. 5, the rotation sensitivity of the comagnetometer operating at the compensation point and the working point is shown. The output signal is demodulated by the lock-in amplifier and acquired by a National Instrument 24-bit data acquisition system with the sampling rate of 200 Hz. The power spectral density is calculated and averaged for each 0.1-Hz bin. The scale factor calibrated by the rotating platform is used to convert the output voltage signal to the rotation rate signal. The rotation sensitivity of each sensitive axis is about 4.2×10^{-7} rad s^{-1} Hz$^{-1/2}$ in the frequency domain above 0.2 Hz. The roll-off at frequencies higher than 30 Hz is due to the cutoff frequency of the lock-in amplifier. Note that the comagnetometer operating at the compensation point and the working point achieves almost the same rotation sensitivity, but when operating at the working point, the cross-talk effect is suppressed, which is vitally important to the navigation application of the comagnetometer. What is more, there is no undesirable peak in the noise spectrum, which illustrates that the stability of the dual-axis comagnetometer is quite good. The angle random walk is about 1.5×10^{-3} deg/h$^{1/2}$. The probe background noise is also obtained in the absence of the pump laser and is about 1.1×10^{-7} rad s^{-1} Hz$^{-1/2}$ above 0.2 Hz, much lower than the rotation rate noise. The polarimetry noise does not limit the rotation sensitivity.

Above 0.2 Hz, the rotation sensing noise of the dual-axis comagnetometer we built is dominated by the ac fluctuation of the ambient magnetic fields. The innermost layer of the

μ-metal magnetic shield is 160 mm long, 100 mm in diameter, and 2 mm thick. According to [27] amd [28], the magnetic noise of the μ-metal magnetic shield is about 31.4 fT/Hz$^{1/2}$ at 1 Hz including the thermal magnetic noise and the eddy current magnetic noise. Then the magnetic noise is suppressed by a factor of 0.6 by the coupled spin ensembles [8], which is consistent with the rotation rate noise. The next generation of the dual-axis comagnetometer will enlarge the innermost layer magnetic shield and a low-noise ferrite magnetic shield will be used, to decrease the magnetic noise.

At low frequencies (<0.2), the rotation sensing noise is limited by $1/f$ noise and other technical sources, including laser beam motion, thermal drift of temperature-sensitive components, residual magnetic field drift, etc. These noises dominate the long-term drift of the dual-axis comagnetometer. Considerable efforts have been made to reduce the low-frequency noises and extend the flat noise-limited region to the low-frequency regime, and a bias drift on the order of 10^{-2} deg/h has been achieved with our dual-axis K-Rb-^{21}Ne comagnetometer.

IV. CONCLUSION

In conclusion, we have theoretically and experimentally examined the cross-talk effect suppression in a compact dual-axis K-Rb-^{21}Ne comagnetometer. The steady-state response of the electron and nuclear spin polarization operated in the SERF regime is investigated considering a large electron magnetic field, and an intuitive model is presented to illustrate the principle of rotation sensing, the cross-talk effect, and its suppression. Due to the nonnegligible fictitious magnetic field of light shift in the K-Rb-^{21}Ne comagnetometer compared to the K-^{3}He comagnetometer, operating at the compensation point, there is an extreme cross-talk effect in the two sensitive axes, which limits the application of the comagnetometer. Here a real magnetic field is used to compensate the light-shift field and operate the comagnetometer at the working point. The feasibility is verified by experiments. With the cross-talk effect suppressed, our dual-axis comagnetometer can carry out high-precision rotation sensing along two sensitive axes simultaneously and independently. This work will be of considerable benefit in equipping the comagnetometer for the inertial navigation system and fundamental physics applications.

Further improvement will be by enlarging the innermost layer magnetic shield and adopting a low-noise ferrite magnetic shield to decrease the magnetic noise, then increase the sensitivity of rotation sensing. Meanwhile, to overcome the limited linear measuring range and suppress the long-term drifts, the closed-loop scheme of the dual-axis comagnetometer is under investigation.

ACKNOWLEDGMENTS

This work was supported by the National Natural Science Foundation of China (Grants No. 61227902, No. 61673041, and No. 61374210) and the National Key R&D Program of China (Grant No. 2016YFB0501600).

---

[1] W. Happer and A. C. Tam, Phys. Rev. A **16**, 1877 (1977).
[2] T. G. Walker and W. Happer, Rev. Mod. Phys. **69**, 629 (1997).
[3] M. Smiciklas, J. M. Brown, L. W. Cheuk, S. J. Smullin, and M. V. Romalis, Phys. Rev. Lett. **107**, 171604 (2011).
[4] V. A. Kostelecký and N. Russell, Rev. Mod. Phys. **83**, 11 (2011).
[5] G. Vasilakis, J. M. Brown, T. W. Kornack, and M. V. Romalis, Phys. Rev. Lett. **103**, 261801 (2009).
[6] M. Bulatowicz, R. Griffith, M. Larsen, J. Mirijanian, C. B. Fu, E. Smith, W. M. Snow, H. Yan, and T. G. Walker, Phys. Rev. Lett. **111**, 102001 (2013).
[7] J. Fang, Y. Chen, S. Zou, X. Liu, Z. Hu, W. Quan, H. Yuan, and M. Ding, J. Phys. B **49**, 065006 (2016).
[8] T. W. Kornack, R. K. Ghosh, and M. V. Romalis, Phys. Rev. Lett. **95**, 230801 (2005).
[9] T. W. Kornack and M. V. Romalis, Phys. Rev. Lett. **89**, 253002 (2002).
[10] R. Li, W. Fan, L. Jiang, L. Duan, W. Quan, and J. Fang, Phys. Rev. A **94**, 032109 (2016).
[11] J. Fang, J. Qin, S. Wan, Y. Chen, and R. Li, Chinese Sci. Bull. **58**, 1512 (2013).
[12] J. Fang, S. Wan, and H. Yuan, Appl. Opt. **52**, 7220 (2013).
[13] G. Renon, N. Zahzam, Y. Bidel, A. Bresson, and P.-J. Nacher, in *APS Division of Atomic, Molecular and Optical Physics Meeting Abstracts*, Vol. 1 (American Physical Society, College Park, MD, 2013), p. 1135.
[14] J. Fang, Y. Chen, Y. Lu, W. Quan, and S. Zou, J. Phys. B **49**, 135002 (2016).
[15] R. K. Ghosh and M. V. Romalis, Phys. Rev. A **81**, 043415 (2010).
[16] E. Babcock, I. Nelson, S. Kadlecek, B. Driehuys, L. W. Anderson, F. W. Hersman, and T. G. Walker, Phys. Rev. Lett. **91**, 123003 (2003).
[17] M. V. Romalis, Phys. Rev. Lett. **105**, 243001 (2010).
[18] Y. Chen, W. Quan, S. Zou, Y. Lu, L. Duan, Y. Li, H. Zhang, M. Ding, and J. Fang, Sci. Rep. **6**, 12 (2016).
[19] T. Juneau, A. Pisano, and J. H. Smith, in *Solid State Sensors and Actuators, 1997. TRANSDUCERS'97 Chicago, 1997 International Conference*, Vol. 2 (IEEE, New York, 1997), pp. 883–886.
[20] J. Qin, J. Fang, and S. Wan, in *Instrumentation and Control Technology (ISICT), 2012 8th IEEE International Symposium* (IEEE, New York, 2012), pp. 24–27.
[21] S. R. Schaefer, G. D. Cates, T.-R. Chien, D. Gonatas, W. Happer, and T. G. Walker, Phys. Rev. A **39**, 5613 (1989).
[22] W. Happer and B. Mathur, Phys. Rev. **163**, 12 (1967).
[23] I. Sulai, R. Wyllie, M. Kauer, G. Smetana, R. Wakai, and T. Walker, Opt. Lett. **38**, 974 (2013).
[24] J. Fang, T. Wang, W. Quan, H. Yuan, H. Zhang, Y. Li, and S. Zou, Rev. Sci. Instrum. **85**, 063108 (2014).
[25] H. Ho, W. Law, S. Wu, X. Liu, S. Wong, C. Lin, and S. Kong, Sensors Actuators B: Chem. **114**, 80 (2006).
[26] L. Duan, J. Fang, R. Li, L. Jiang, M. Ding, and W. Wang, Opt. Express **23**, 32481 (2015).
[27] J. Nenonen, J. Montonen, and T. Katila, Rev. Sci. Instrum. **67**, 2397 (1996).
[28] S.-K. Lee and M. Romalis, J. Appl. Phys. **103**, 084904 (2008).